A micromagnetic study of the reversal mechanism in permalloy antidot arrays

B. Van de Wiele, A. Manzin, A. Vansteenkiste, O. Bottauscio, L. Dupré et al.

Citation: J. Appl. Phys. **111**, 053915 (2012); doi: 10.1063/1.3689846
View online: http://dx.doi.org/10.1063/1.3689846
View Table of Contents: http://jap.aip.org/resource/1/JAPIAU/v111/i5
Published by the American Institute of Physics.

A micromagnetic study of the reversal mechanism in permalloy antidot arrays

B. Van de Wiele,[1,a)] A. Manzin,[2] A. Vansteenkiste,[3] O. Bottauscio,[2] L. Dupré,[1] and D. De Zutter[4]
[1]*Department of Electrical Energy, Systems and Automation, Ghent University, Sint Pietersnieuwstraat 41, B-9000 Ghent, Belgium*
[2]*Istituto Nazionale di Ricerca Metrologica, Strada delle Cacce 91, 10135, Italy*
[3]*Department of Solid State Sciences, Ghent University, Krijgslaan 281-S1, B-9000 Gent, Belgium*
[4]*Department of Information Technology, Ghent University, Sint Pietersnieuwstraat 41, B-9000 Ghent, Belgium*

(Received 3 October 2011; accepted 1 February 2012; published online 7 March 2012)

A numerical analysis is focused on the influence of patterning and finite-size effects on the hysteresis properties and magnetization reversal of permalloy antidot films with square lattice and square holes. Simulations are performed by solving the Landau-Lifshitz equation. The aim is to explain the relationships between the shape of the hysteresis loop and the different stages of the reversal process. In particular, the switching mechanism is characterized by the nucleation of domain chains that destroy the periodic symmetry in the magnetization present when infinite periodicity is considered. This behavior is strongly influenced by the demagnetizing effects arising both at the film boundaries and at the hole edges. © *2012 American Institute of Physics*. [http://dx.doi.org/10.1063/1.3689846]

I. INTRODUCTION

Recently, there has been growing interest in the fabrication, characterization, and modeling of magnetic antidot arrays (i.e., periodic arrays of nonmagnetic inclusions in magnetic media) to investigate their potential application in ultrahigh-density magnetic recording, information processing, and magnetic sensing.[1–3] Specific attention has been devoted to recording processes, studying the magnetic domain configuration at the remanent state to obtain small isolated regions where the basic unit of information could be stored.[4–8] Magnetotransport and hysteresis properties have been investigated in detail, considering different materials and analyzing the role of lattice configuration, hole shape, and geometrical parameters, such as the hole size and the interhole distance.[9–23] Magnetic domain structures arising in antidot arrays have been experimentally observed by means of magnetic force microscopy (MFM), Lorentz microscopy, X-ray photoemission electron microscopy, and magneto-optic Kerr effect measurements.[22–29] The patterning introduces a spatially dependent shape anisotropy that allows the nucleation and propagation of domain walls, influencing in this way the reversal mechanism, the remanent magnetization, and the coercive field.[9–16] A fourfold anisotropy has been found in square-lattice geometries, while hexagonal and honeycomb configurations exhibit a sixfold symmetry.[9] Particular attention has been devoted to the nucleation and propagation of discrete domain chains, to explore the possibility of controlling domain walls with well-defined magnetic configurations.[30–32] Other important efforts have been made to investigate dynamic properties, focusing on ferromagnetic resonance phenomena and spin-wave propagation for possible application in magnetic logic devices.[33–41]

A fundamental support to understand the complex magnetic behavior of antidot arrays has been found in micromagnetic simulations based on the solution of the Landau-Lifshitz equation.[42,43] To limit the computational time and the memory requirements, the micromagnetic simulations have often been performed by introducing periodic boundary conditions on the edges of the unit cell that defines the spatial period. This simplifying approach is based on the hypotheses of exact geometrical and physical periodicity (e.g., absence of lattice defects), infinite dimensions along the patterning plane, and spatially uniform applied field. In this way, the global shape anisotropy as well as the domain wall pinning at crystal defects and effective edges of the entire magnetic medium are neglected. As depicted in Refs. 30 and 31, the reversal mechanism occurs by nucleation and propagation of domain chains. Consequently, the spatial distribution of the magnetization presents a local behavior that is far from spatial periodicity.

The aim of this paper is to investigate, through a micromagnetic numerical approach, the hysteresis properties and the reversal mechanism of permalloy antidot thin films with square lattice and square holes. Films with global dimensions of the order of some micrometers are considered, to study the influence of boundary effects and to reproduce the actual experimental conditions that cannot be simulated by introducing infinite periodicity. According to several studies, the square-lattice geometry leads to a fourfold anisotropy with the hard axes parallel to the edges of the holes and the easy ones along the diagonal directions. As outlined in Ref. 9, the hysteresis loops measured along the easy directions have a higher remanent magnetization and present a sharp switching in correspondence of the coercive field. On the contrary, the hysteresis loops measured along the hard directions are

a)Author to whom correspondence should be addressed. Electronic mail: ben.vandewiele@ugent.be.

characterized by kinks and present a more gradual switching with lower values of the remanent magnetization and the coercive field.

In this paper, the reversal mechanism along the hard axis direction is analyzed to provide a physical interpretation of the particular shape of the hysteresis loop. Despite several works that dealt with the experimental and numerical analysis of static properties, no detailed micromagnetic studies of the switching mechanism has been performed so far, taking into account both patterning and boundary effects.

The paper is organized as follows. Section II briefly describes the simulation methodology and the sample specifications. The results of the numerical study and discussion of those results are presented in Secs. III and IV, while final conclusions are in Sec. V. In particular, Sec. III is devoted to the influence of finite-size effects, hole size, and hole shape on the global hysteresis behavior along the hard-axis directions. In Sec. IV the reversal mechanism is investigated in detail, considering magnetization configurations at different points of the hysteresis loop.

II. SIMULATION PROCEDURE AND SAMPLE SPECIFICATIONS

The micromagnetic model is developed in a magnetic antidot film with square lattice and finite size along the x- and y-axes, integrating the Landau-Lifshitz equation,

$$\frac{\partial \mathbf{M}}{\partial t} = -\frac{\gamma_G}{1+\alpha^2}\left[\mathbf{M}\times\mathbf{H}_{\text{eff}} + \frac{\alpha}{M_s}\mathbf{M}\times(\mathbf{M}\times\mathbf{H}_{\text{eff}})\right]. \quad (1)$$

In Eq. (1), γ_G is the absolute value of the gyromagnetic ratio, α is the damping constant, and M_S is the saturation magnetization. The effective field $\mathbf{H}_{\text{eff}}$ is the sum of the applied external field, the anisotropy field, the exchange field, and the magnetostatic field. To compute the hard-axis hysteresis loop, the external field is applied along the x-direction, parallel to one of the edges of the antidot array (see Fig. 1).

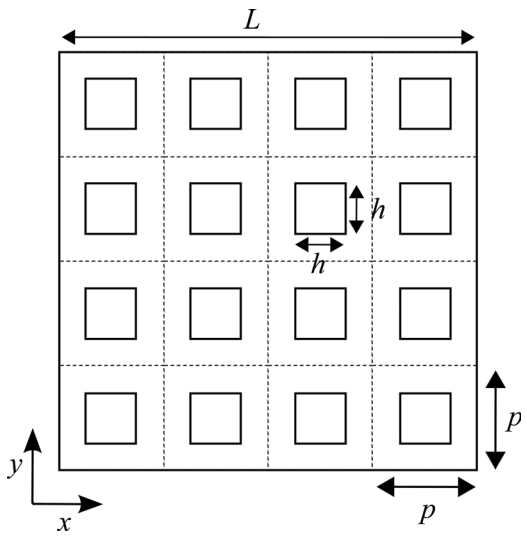

FIG. 1. Scheme of the antidot array with square lattice and square holes. The dashed lines define the unit cells with fixed dimension $p = 200$ nm. The hole size h and the film dimension L are varied in the simulations.

The sample is initially saturated along the positive x-direction by imposing an external field of 200 kA/m. To compute the descending branch of the hysteresis loop, the external field—approximated by a staircase function—is decreased down to −200 kA/m considering 500 constant values. For each step of the applied field, the system is relaxed toward the corresponding equilibrium point by time integrating Eq. (1). The equilibrium point is supposed to be reached when the change in the Gibbs free energy has reached the numerical noise level. At that moment, a next step on the applied field is imposed.

The sample material is permalloy with saturation magnetization $M_S = 860$ kA/m, exchange constant $k_{ex} = 13$ pJ/m, and negligible magnetocrystalline anisotropy. The attention is focused on antidot films with in-plane dimension $L \times L$ and thickness equal to 20 nm. The structures are characterized by a square lattice and, if not differently specified, contain square holes with variable size h. The spatial period p (i.e., the dimension of the square unit cell) is kept constant at 200 nm in all simulations. The samples are discretized using a 2D grid containing finite difference cells of size $3.125 \times 3.125 \times 20$ nm^3, providing a resolution in the xy-plane lower than the exchange length. The simulations are performed using the software package MUMAX,[44] which runs on Graphics Processing Units (GPUs), providing a computational speedup of up to two orders of magnitude compared to standard CPUs. This has allowed us to treat large antidot arrays in an acceptable computation time while maintaining a fine space resolution. On one of the eight nVIDIA GTX580 GPUs used for the analysis, the computation of one branch of the hysteresis loop of an antidot array with $L = 3.2\,\mu$m (1024×1024 finite difference cells) requires typically 2 h and 15 min.

III. STUDY OF HYSTERESIS PROPERTIES

A. Influence of finite-size effects

The role of finite-size effects on the shape of the hard-axis hysteresis loop is investigated by varying parameter L, which represents the global film dimension in the xy-plane (Fig. 1). The hole size is set at 100 nm. By increasing L, the descending branches of the hysteresis loops have an asymptotic behavior toward a limit curve (see Fig. 2). Moreover, Fig. 3 shows that, for sample dimension $L < 16p$, when increasing L, the coercive field decreases due to the reduction of the in-plane demagnetizing field, while the remanent magnetization increases if L is an odd multiple of p, and reduces if L is an even multiple of p. In the latter case, the remanent magnetization is higher because the system is perfectly symmetric and, thus, characterized by a higher stiffness. When L is higher than $16p$ ($L = 3.2\,\mu$m in the analyzed case) no appreciable variations are observed in the remanent magnetization and coercive field. Thus, to study the hysteresis properties and interpret the reversal mechanism, the results obtained for antidot arrays of size $L = 16p$ are representative for antidot arrays with larger dimensions. Hence, samples with dimension $L = 16p$ are considered in all the following simulations.

As a comparison, the hysteresis loop has also been computed by imposing periodicity conditions in correspondence

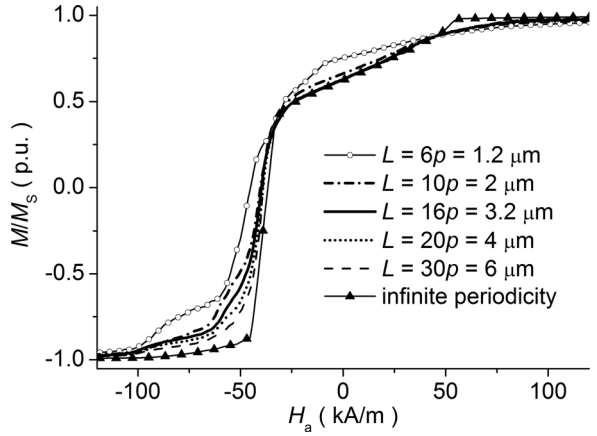

FIG. 2. Descending branches of the hard-axis hysteresis loops computed for variable sample size L. The hole size h is 100 nm and the spatial period p is 200 nm. The curve computed with periodic boundary conditions is reported for comparison.

of the boundaries of a macrocell including 16×16 unit cells. As put in evidence in Fig. 2, the limit hysteresis loop obtained by increasing L does not coincide with the one calculated with infinite periodicity conditions. This is a consequence of the differences found in the spatial distribution of the magnetization and in the reversal mechanism. In the infinite film the magnetization distribution is identical in each unit cell, giving rise to a switching process characterized by a leaf configuration around each hole.[7,30] In finite-sized films, local demagnetizing effects arise at the sample boundaries, strongly affecting the overall reversal process, which is characterized by the formation of magnetic domain chains. A detailed description will be given in Sec. IV.

B. Influence of hole size

By increasing h, the remanent magnetization reduces and the coercive field increases (Fig. 4). These results are in agreement with the ones found both experimentally and numerically in previous papers for a square lattice configuration.[5,7,14,16] In particular, the system obeys the well-known

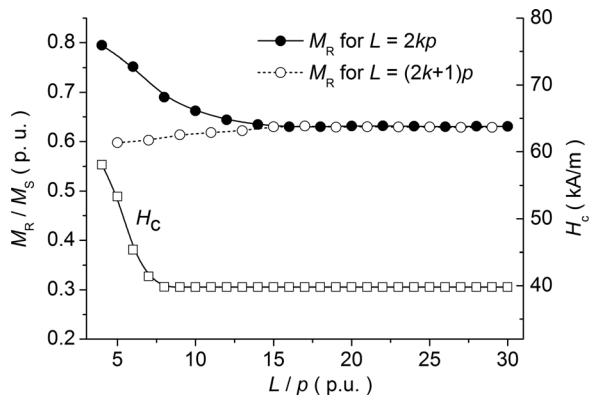

FIG. 3. Remanent magnetization and coercive field vs sample size L, for an antidot array with square lattice and square holes. To distinguish the behaviors of the remanent magnetization found when L is an odd/even multiple of p, the integer number k is introduced. The hole size h is 100 nm and the spatial period p is 200 nm.

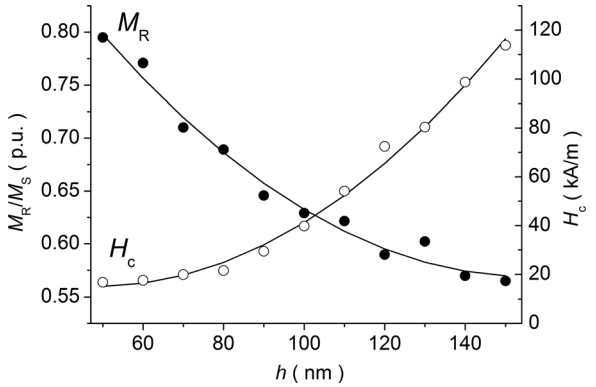

FIG. 4. Remanent magnetization and coercive field vs hole size h, for an antidot array with square lattice and square holes. The spatial period p is 200 nm and the sample size L is 3.2 μm.

phenomenological linear relationship between the coercive field and the geometrical parameter $1/(p-h)$.[16] This result confirms that the variation in the coercive field is mainly due to the change in the spatial distribution of the local demagnetizing field induced by the presence of holes. In fact, the smaller the distance between the closest holes $(p-h)$, the higher the external field necessary to counteract the dipolar fields and the domain wall pinning effects over the antidot array.

Figure 5 compares the descending branches of the hysteresis loops computed for h equal to 80 nm, 100 nm, and 120 nm to those of the unpatterned film. When inspecting the loops of the patterned films, six different stages (A to F) can be distinguished in the switching process, suggesting similar reversal mechanisms in all samples. The antidot array with the lowest packing fraction ($h = 80$ nm) has the weakest local shape anisotropy induced by patterning. Consequently, the corresponding loop is most similar to the one of the continuous film.

The computed hysteresis loops present strong analogies to the ones found experimentally for antidot arrays with the same lattice configuration and comparable packing fraction, see for example the loops in Fig. 4(b) of Ref. 9 and in Fig. 2(a) of Ref. 22, measured by vibrating sample magnetometer (VSM) and magneto-optic Kerr effect (MOKE), respectively. Specifically, they are characterized by a gradual switching in the magnetization and by three kinks, occurring at the beginning of the reversal process, at the coercive field and before reaching saturation in the negative direction.

C. Influence of hole shape

As previously depicted, the computed hysteresis loops present strong similarities in shape with the ones obtained in other papers for the same lattice configuration and comparable hole density, even if some differences in the coercive field and in the first stage of the reversal process can be found.[9,22,27,37] This can be due to differences in the magnetocrystalline anisotropy of the sample material, in the hole shape and size, and in the spatial period. As an example, the hole shape has a strong influence on the coercive field and remanent magnetization values. As shown in Fig. 6, the presence of circular holes instead of square ones leads to a higher

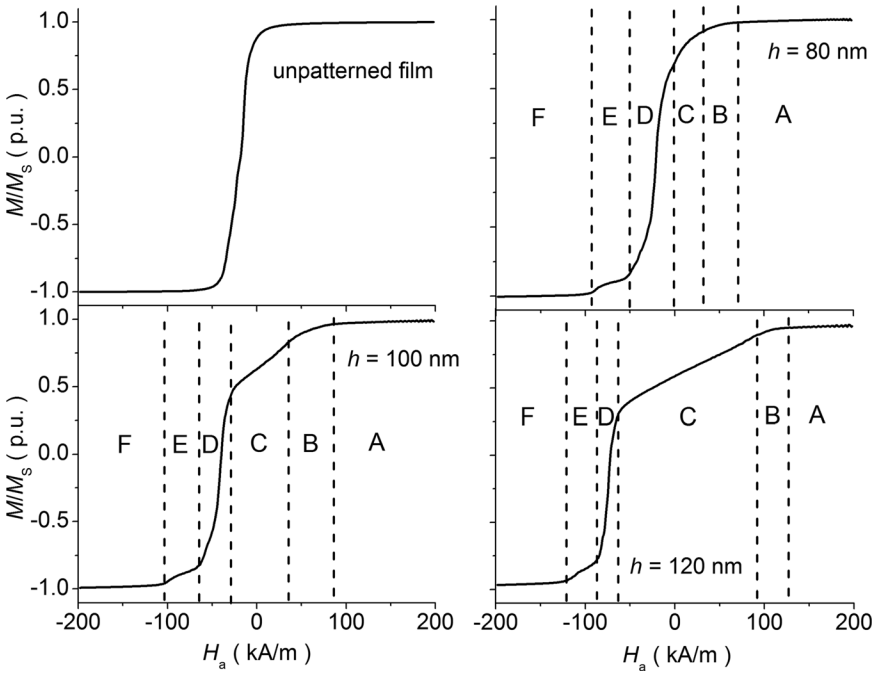

FIG. 5. Descending branches of the hard-axis hysteresis loops computed for antidot arrays with square lattice and variable hole size h. The hysteresis loop for the unpatterned film is reported for comparison. The spatial period p is 200 nm and the sample size L is 3.2 μm.

squareness and a lower coercivity, as a consequence of the elimination of the local anisotropy contribution due to sharp corners. In particular, the coercive field is approximately halved. An intermediate behavior can be found by considering holes with rounded corners.

IV. STUDY OF THE REVERSAL MECHANISM

The reversal mechanism along the hard-axis direction is investigated in detail, focusing on the six stages identified in Fig. 5 and on the role of the hole size, h. The antidot structures with packing fractions $h/p = 0.4$, 0.5, and 0.6 are treated (i.e., h equal to 80 nm, 100 nm, and 120 nm). As mentioned before, antidot arrays with global size $L = 16p$ are considered. Although not presented here, we confirm that the same stages in the hysteresis loops and internal magnetization processes are observed in antidot arrays with the same spatial period, but higher global dimensions.

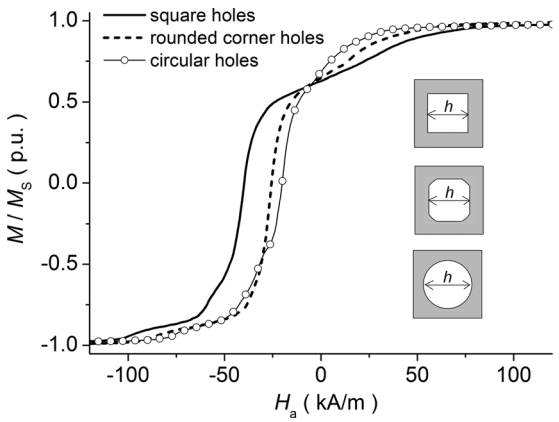

FIG. 6. Descending branches of the hard-axis hysteresis loops computed for an antidot array with square lattice and variable hole shape (i.e., square, circular, and rounded corner). For each shape, the hole size is set at 100 nm.

A. Intermediate packing fraction (h/p = 0.5)

Figure 7 shows representative magnetization configurations in each of the six stages for the antidot array with hole size $h = 100$ nm. Here and in all the successive magnetization plots, the color code presented in Fig. 8 is used to represent the local magnetization direction. To explain the reversal process we will concentrate on unit cells in the top-right quadrant of the antidot array.

In *stage A*, the sample is almost completely saturated. As a result of global demagnetizing effects, the magnetization near the outer left and right sample edges rotates in the vertical direction. Furthermore, some local magnetization rotation takes place near the left and right edges of all holes due to the local demagnetizing effects introduced by the patterning.

In *stage B*, as a result of the global demagnetizing field, the magnetization configuration throughout the sample is subdivided into four quadrants. In each quadrant two phenomena are visible: (i) the magnetization at the intersections of the columns and rows turns toward the 45° directions and (ii) in the columns, the magnetization gradually aligns with the hole edges to minimize the local demagnetizing fields leading to an S-state, also observed in transmission X-ray microscopy (TXM) images reported in Ref. 45. The two effects are visible in Fig. 9, stage B, which shows a zoom of the spatial distribution of the magnetization around a hole located in the top-right quadrant. In each quadrant of the sample, the direction to which the magnetization turns (i.e., positive or negative y-axis) is imposed by the global demagnetizing phenomena. The magnetization pattern shown in Fig. 9, stage B, appears first around the holes at the corners of the antidot array and then gradually moves toward the sample center. This is a reversible magnetization process. In the sample center, between the holes, there is the formation of a flower state with four spikes, also reported in Ref. 45.

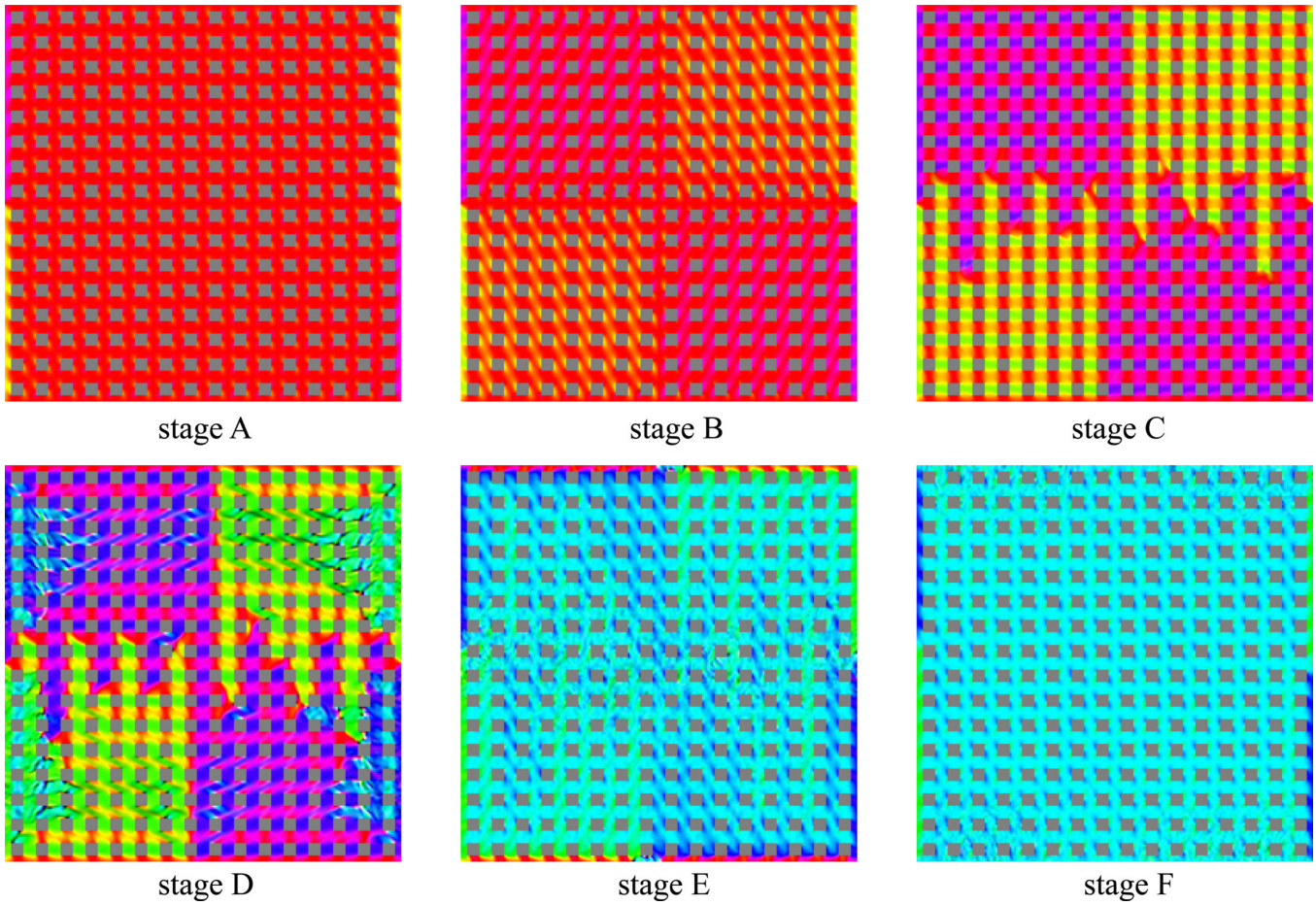

FIG. 7. (Color online) Snapshots of the magnetization at different points of the descending branch of the hysteresis loop for the antidot array with $L = 3.2\,\mu$m and $h = 100$ nm. The stages refer to those defined in Fig. 5.

In *stage C*, the magnetization in the columns rotates from the positive x-axis (see stage B) toward the positive or negative y-axis. Here, the two dominant competing energy terms are the Zeeman and the demagnetizing energy. Although the external field tries to keep the magnetization aligned with the x-axis, the local demagnetizing effects try to rotate the magnetization toward the vertical directions. Because the external field is slowly varied, the result is a reversible coherent rotation of the magnetization. This explains the gradual decrease of the average magnetization seen in the hysteresis loop branch reported in Fig. 5. At the remanent state, the so called leaf type configuration[7,30] is reached as shown in Fig. 9, stage C. At the end of this rotation process, magnetization chains are formed, as also found in Ref. 30 (see Fig. 7, stage C).

In *stage D*, the magnetization in the rows switches from the positive to the negative x-direction. This is an irreversible magnetization process. By inspecting Fig. 7, stage D, one can observe that there are portions of the antidot array that are at different phases of the reversal process. In particular, four different phases can be distinguished. Figure 9, stages D1 to D4, show representative unit cells for each phase. All the considered cells are chosen from the top-right quadrant. Note that in this plot, the system is not yet in equilibrium.

(1) In the top-right quadrant, the rows closest to the film boundaries are mainly oriented along the x-axis (Fig. 7, stage D, red color). These rows have only started the switching process. Figure 9, stage D1, shows that at the intersections of the columns and rows the magnetization is still aligned with the 45° directions, as in stage B. In the center of the top row, the magnetization is starting to rotate away from the x-axis, while in the bottom row, no rotation has taken place yet. In this phase, the magnetization near the antidot edges is still aligned with the hole boundaries to minimize the local demagnetizing fields.
(2) Some rows in Fig. 7, stage D, are partially aligned with the positive y-axis (green color). They are at an intermediate phase in the switching process. Figure 9, stage D2, shows how the magnetization in the center of the row continues the in-plane rotation process from the positive to the negative x-axis. A large component along the positive y-axis, indicated by the green color, is present. The magnetization near the hole boundaries starts to switch

FIG. 8. (Color online) Color code used for plotting the magnetization configurations. The black and white colors are proportional to the magnetization component pointing into and out of the sheet, respectively.

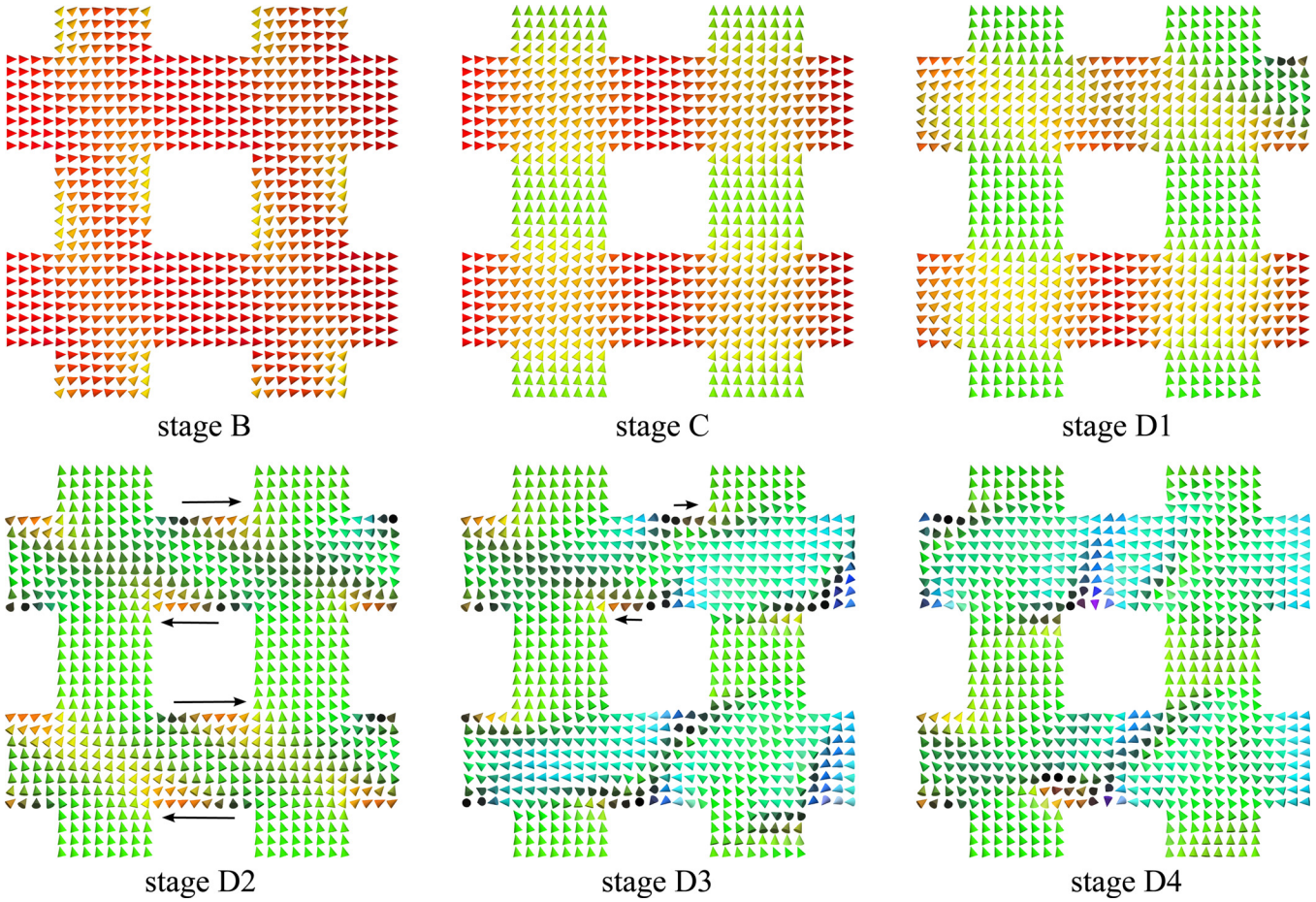

FIG. 9. (Color online) Zooms into the magnetization plots of Fig. 7. Each arrow represents a local average of 4×4 magnetization vectors.

by means of an out-of-plane reversal mechanism: small out-of-plane magnetized regions separating positively and negatively magnetized areas move along the hole boundaries. This movement is depicted with an arrow: at the top boundary the out-of-plane magnetized region moves from right to left and vice versa at the bottom, leading to the reversal of the magnetization near the hole boundaries. In the top-left and bottom-right quadrants of the sample, the small out-of-plane regions move in the opposite direction.

(3) Some rows in Fig. 7, stage D, are characterized by an out-of-plane magnetized region oriented along diagonal directions (black diagonal stripes). A zoom of this configuration is given in Fig. 9, stage D3. In the top row, the reversal near the antidot edges is still taking place, indicated by the arrows. In the center of this row, the area with a magnetization having a large component along the y-axis (i.e., arrows with a green color) is decreasing. The switched areas (blue color) and non-switched ones (green color) are separated by a well-localized line originating at the moving out-of-plane magnetized regions near the antidot edges. In this "domain wall" the magnetization rotates in a coherent in-plane way from the vertical direction to the negative x-axis. In the bottom row, the switching near the antidot boundaries has ended. The non-switched (green) area has completely disappeared and the two small out-of-plane regions have reached the opposite hole corners. Both these regions are now connected by a transverse domain wall, which has a large out-of-plane magnetization component that gives rise to the black colored stripes in Fig. 7, stage D. It should be noted that this domain wall is smoothed out in the representation of Fig. 9, stage D3, because each arrow represents the average magnetization of 4×4 finite difference cells in the simulation.

(4) Some rows in Fig. 7, stage D, are partially oriented along the negative x-axis (blue color). In these rows, the annihilation of the transverse domain walls indicates the end of the reversal process (Fig. 9, stage D4).

Stage E is the counterpart of stage B. The same configuration is present: (i) the magnetization in the outer parts of the columns is aligned with the hole edges in order to minimize local demagnetizing fields, while the central parts are already rotated toward the negative x-direction and (ii) the magnetization at the intersections is aligned with the 45° directions. The rows at the top and bottom edges of the antidot array are still magnetized along the positive x-direction (see Fig. 7, stage E).

Finally, at *stage F*, the magnetization at the intersections of the columns and rows and at the left and right antidot edges has switched as well. In Fig. 7, stage F, only the outer left and right boundaries of the samples still have a

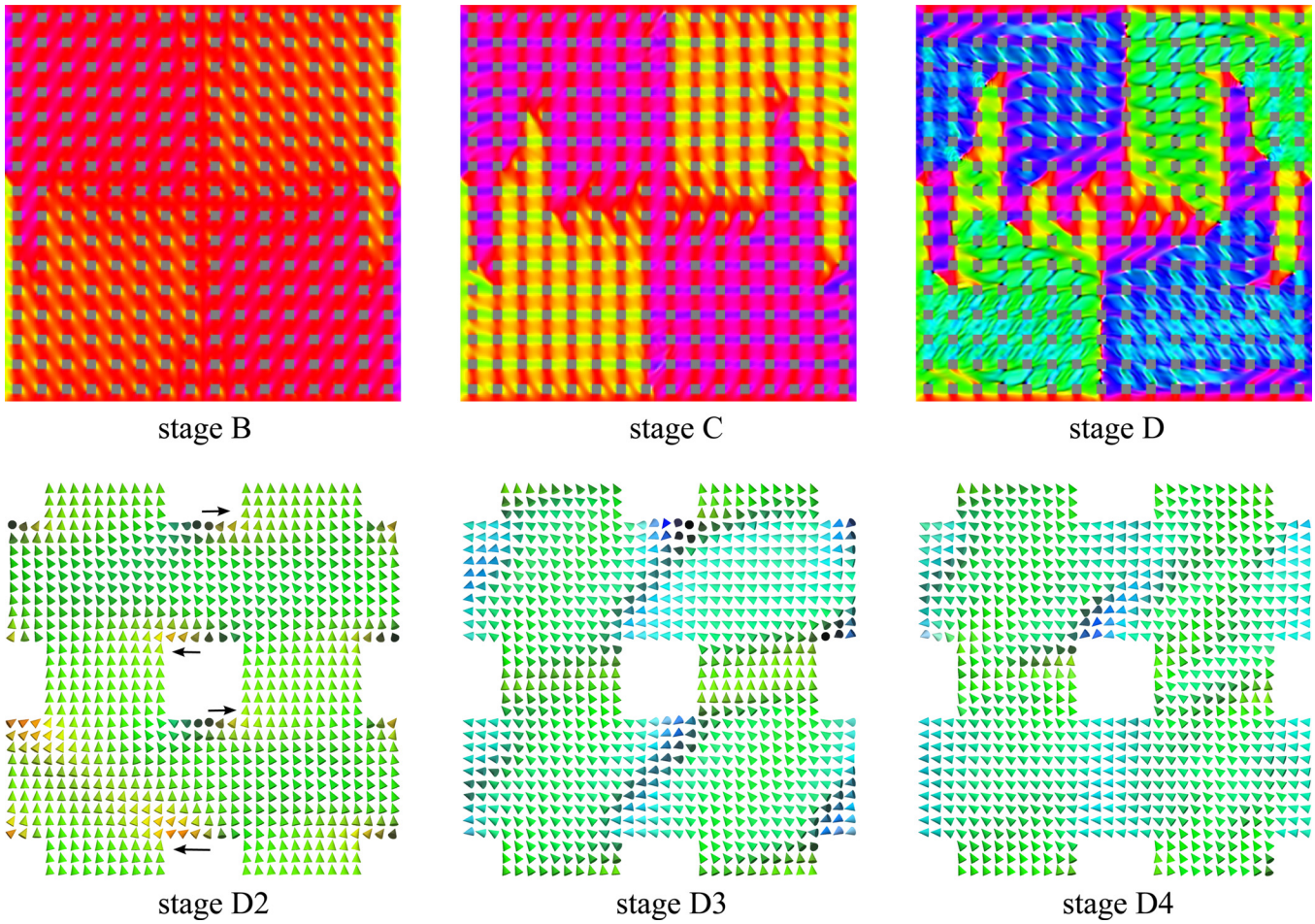

FIG. 10. (Color online) Top row: snapshots of the magnetization at different points of the descending branch of the hysteresis loop for the antidot array with $L = 3.2\ \mu$m and $h = 80$ nm. The stages refer to those defined in Fig. 5. Bottom row: zooms into the magnetization configurations of stage D.

magnetization in the y-direction. Now, the magnetization in the rows at the top and bottom edges of the antidot array is oriented along the negative x-axis. This explains the jump in the hysteresis loop between stages E and F (see Fig. 5).

B. Low packing fraction (h/p = 0.4)

In Fig. 10, the antidot array with hole size equal to 80 nm is considered. The comments are supported by snapshots for representative points of the hysteresis loop at stages B, C, and D (top) and zooms into the magnetization state in some unit cells at different reversal phases in stage D (bottom). In *stages A, B, E*, and *F* similar reversal processes to the case $h/p = 0.5$ are found. Hence, we will not treat these stages in detail, but concentrate on the other ones. Again, we will consider only cells in the top-right quadrant.

From Fig. 5 it is clear that *stage C* extends over a smaller range of the applied field than it does in the $h/p = 0.5$ case. However, the same phenomena appear: the magnetization in the inner parts of the columns rotates coherently from the positive x-axis toward the positive or negative y-axis (the magnetization near the left and right antidot boundaries was already rotated at stage B). As a result of the larger width of the magnetic regions, the local demagnetizing effects are weaker. Consequently, only in a smaller range of external field values, the demagnetizing energy can compete with the Zeeman energy to rotate the magnetization toward the y-direction.

The irreversible switching mechanism in the rows at *stage D* slightly differs from that of the $h/p = 0.5$ case. Except for the unit cells at the sample boundaries, no coexistence of magnetic regions that have not started the reversal process and regions that are in the switching process is observed. The reason is that the magnetization is less pinned along the x-direction due to the larger width of the magnetic regions.

The reversal of the rows is still characterized by the movement (in opposite directions) of small out-of-plane magnetized regions (see Fig. 10, stage D2). Also here, a transverse domain wall is formed when the out-of-plane magnetized regions arrive at the opposite hole corners (Fig. 10, stage D3). In this case, the domain wall has a better defined structure because less energy is confined inside it. Indeed, due to the wider magnetic regions, the spatial variation of the magnetization is much smoother, giving rise to lower exchange energies. This is also clear from Fig. 10, stage D4, which shows a snapshot of the annihilation process of the transverse domain wall. This process is much less chaotic than in the $h/p = 0.5$ case, because a smaller amount of energy is confined in the domain wall and the magnetic regions are wide enough to allow the energy dissipation in a more gradual way.

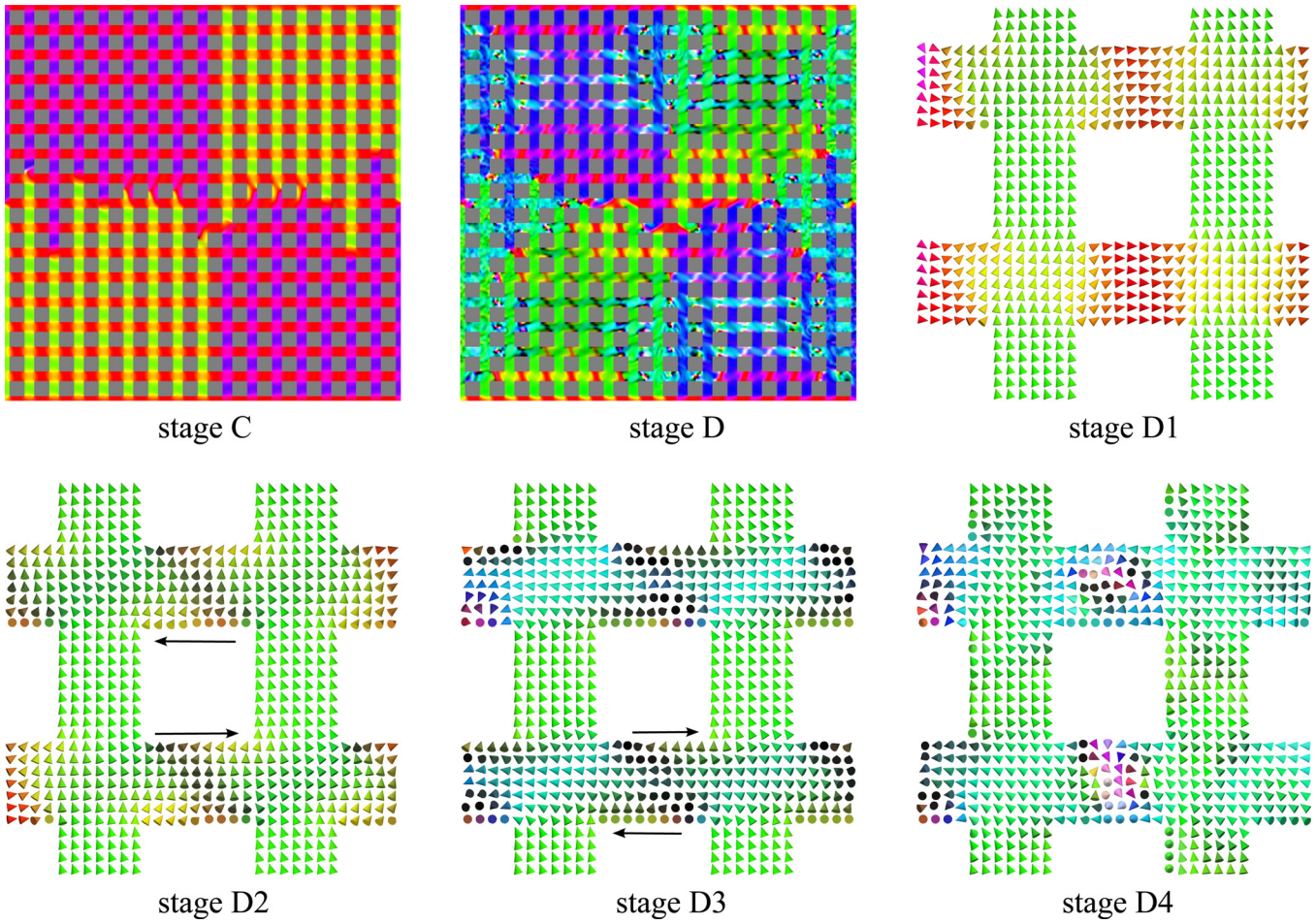

FIG. 11. (Color online) Top row (left and middle): snapshots of the magnetization at different points of the descending branch of the hysteresis loop for the antidot array with $L = 3.2\ \mu$m and $h = 120$ nm. The stages refer to those defined in Fig. 5. Top row (right) and bottom row: zooms into the magnetization configurations of stage D.

C. High packing fraction (h/p = 0.6)

Figure 11 shows snapshots for representative points of the hysteresis loop at stages C and D and zooms into the magnetization state in some unit cells of stage D for the antidot array with hole size $h = 120$ nm. In *stages A, B, E*, and *F*, phenomena similar to the $h/p = 0.5$ case are found. Hence, we will concentrate on the other stages.

The *stage C* extends over a broader range of the applied field than in the $h/p = 0.5$ case. The local demagnetizing effects are much stronger due to the narrower magnetic regions. Consequently, the demagnetizing energy can compete with the Zeeman energy over a much broader range of external field values in order to rotate the magnetization from the x-axis toward the y-axis.

During *stage D*, the reversal of the magnetization in the rows is still characterized by four phases. Because in this case the magnetization is much more pinned along the x-direction, rows in which the magnetization reversal has not been started can coexist longer with rows in which the reversal process has started (see Fig. 11, stage D1). This also explains the much larger coercive field values.

The reversal process in the rows starts in the same way as for the $h/p = 0.5$ case. Out-of-plane magnetized regions appear at the top and bottom antidot edges in opposite corners. From Fig. 11, stage D2, it is clear that the area between the two regions has an out-of-plane component as well. Indeed, the magnetic regions are too narrow to enable a completely in-plane rotation as encountered in the $h/p = 0.5$ case. In the snapshot shown in Fig. 11, stage D, these rows are partially oriented along the positive y-axis (green color with a top-left to bottom-right darker region).

When the out-of-plane regions near the antidot boundaries move along the edges, the internal area with an out-of-plane component gradually decreases (Fig. 11, stage D3). Consequently, the magnetization is forced to vary on a reduced space scale, leading to an increased energy density in this area. This is the reason for the growing out-of-plane magnetization component. At a certain point, the energy is concentrated in such a small area that highly chaotic magnetization relaxation phenomena take place, leading to the dissipation of all accumulated energy (Fig. 11, stage D4). After this, the magnetization in the row is completely reversed.

V. CONCLUSIONS

The analysis puts in evidence the role of patterning and finite-size effects on the hysteresis properties and magnetization switching in permalloy antidot films with square holes and square lattice. The hysteresis loops along the hard

magnetization direction have been computed by varying the global sample dimension and the hole size. The shape of the simulated hysteresis loops presents strong similarities to the ones experimentally obtained for antidot arrays with the same lattice configuration. In particular, six stages can be distinguished in the reversal process. From a detailed investigation of the spatial configuration of the magnetization at different points of the hysteresis loop, it is clear that the strength of the local shape anisotropy introduced by the holes largely affects the reversal process and, thus, the hysteresis properties. Furthermore, also finite-size effects influence the magnetization states. In particular, the global demagnetizing fields at the sample boundaries determine the preferred directions for the magnetization rotation in the columns oriented perpendicularly to the applied field. Thus, the global demagnetizing effects are at the basis of the formation of the four equivalent quadrants in the magnetization configuration as well as the magnetic domain chains orthogonal to the external field. Finally, the spatial magnetization distribution is strongly different from the one computed when considering infinite periodicity, even if similar values of the remanent magnetization and coercive field are obtained.

ACKNOWLEDGMENTS

This work has been developed under the EU Project JRP IND 08 "Metrology for Advanced Industrial Magnetics (MetMags)". The EMRP is jointly funded by the EMRP participating countries within EURAMET and the European Union. Furthermore, the work is supported by FWO project G.0142.08.

[1]A.O. Adeyeye and N. Singh, J. Phys. D: Appl. Phys. **41**, 153001 (2008).
[2]R. Skomski, J. Phys.: Condens. Matter **15**, R841 (2003).
[3]C. A. Ross, Annu. Rev. Mater. Res. **31**, 203 (2001).
[4]J. Guo and M. B. A. Jalil, J. Magn. Magnetic Mater. **272–276**, 722 (2004).
[5]M. B. A. Jalil, J. Appl. Phys. **93**, 7053 (2003).
[6]L. Torres, L. Lopez-Diaz, and O. Alejos, J. Appl. Phys. **87**, 5645 (2000).
[7]L. Torres, L. Lopez-Diaz, and J. Iñiguez, Appl. Phys. Lett. **73**, 3766 (1998).
[8]R. P. Cowburn, A. O. Adeyeye, and J. A. C. Bland, J. Magn. Magn. Mater. **173**, 193 (1997).
[9]C. C. Wang, A. O. Adeyeye, and N. Singh, Nanotechnology **17**, 1629 (2006).
[10]A. Pérez-Junquera, J. I. Martín, M. Vélez, J. M. Alameda, J. V. Anguita, F. Briones, E. M. González, and J. L. Vicent, Nanotechnology **15**, S131 (2004).
[11]M. T. Rahman, N. N. Shams, C. H. Lai, J. Fidler, and D. Suess, Phys. Rev. B **81**, 014418 (2010).
[12]K. R. Pirota, P. Prieto, A. M. J. Neto, J. M. Sanz, M. Knobel, and M. Vasquez, J. Magn. Magn. Mater. **320**, e235 (2008).
[13]D. Navas, M. Hernández-Vélez, M. Vázquez, W. Lee, and K. Nielsch, Appl. Phys. Lett. **90**, 192501 (2007).
[14]J. M. Torres Bruna, J. Bartolomé, L. M. García Vinuesa, F. Garcia Sanchez, J. M. Gonzalez, and O. A. Chubykalo-Fesenko, J. Magn. Magn. Mater. **290–291**, 149 (2005).
[15]F. J. Castaño, K. Nielsch, C. A. Ross, J. W. A. Robinson, and R. Krishnan, Appl. Phys. Lett. **85**, 2872 (2004).
[16]I. Ruiz-Feal, L. Lopez-Diaz, A. Hirohata, J. Rothman, C. M. Guertler, J. A. C. Bland, L. M. Garcia, J. M. Torres, J. Bartolome, F. Bartolome, M. Natali, D. Decanini, and Y. Chen, J. Magn. Magn. Mater. **242–245**, 597 (2002).
[17]T.-J. Meng, J.-B. Laloë, S. N. Holmes, A. Husmann, and G. A. C. Jones, J. Appl. Phys. **106**, 033901 (2009).
[18]P. Tiberto, L. Boarino, F. Celegato, M. Coïsson, N. De Leo, F. Vinai, and P. Allia, J. Appl. Phys. **107**, 09B502(2010).
[19]D. Tripathy and A. O. Adeyeye, Phys. Rev. B **79**, 064413 (2009).
[20]C. C. Wang, A. O. Adeyeye, N. Singh, Y. S. Huang, and Y. H. Wu, Phys. Rev. B **72**, 174426 (2005).
[21]A. O. Adeyeye, J. A. C. Bland, and C. Daboo, Appl. Phys. Lett. **70**, 3164 (1997).
[22]N. G. Deshpande, M. S. Seo, X. R. Jin, S. J. Lee, Y. P. Lee, J. Y. Rhee, and K. W. Kim, Appl. Phys. Lett. **96**, 122503 (2010).
[23]P. Vavassori, G. Gubbiotti, G. Zangari, C. T. Yu, H. Yin, H. Jiang, and G. J. Mankey, J. Appl. Phys. **91**, 7992 (2002).
[24]R. H. Cheng, B. L. Justus, A. Rosenberg, D. N. McIlroy, Z. Holman, D. Zhang, and Y. Kranov, J. Appl. Phys. **108**, 086110 (2010).
[25]E. T. Papaioannou, V. Kapaklis, P. Patoka, M. Giersig, P. Fumagalli, A. Garcia-Martin, E. Ferreiro-Vila, and G. Ctistis, Phys. Rev. B **81**, 054424 (2010).
[26]L. J. Heyderman, F. Nolting, and C. Quitmann, Appl. Phys. Lett. **83**, 1797 (2003).
[27]I. Guedes, M. Grimsditch, V. Metlushko, P. Vavassori, R. Camley, B. Ilic, P. Neuzil, and R. Kumar, Phys. Rev. B **66**, 014434 (2002).
[28]U. Welp, V. K. Vlasko-Vlasov, G. W. Crabtree, C. Thompson, V. Metlushko, and B. Ilic, Appl. Phys. Lett. **79**, 1315 (2001).
[29]A. Y. Toporov, R. M. Langford, and A. K. Petford-Long, Appl. Phys. Lett. **77**, 3063 (2000).
[30]L. J. Heyderman, F. Nolting, D. Backes, S. Czekaj, L. Lopez-Diaz, M. Kläui, U. Rüdiger, C. A. F. Vaz, J. A. C. Bland, R. J. Matelon, U. G. Volkmann, and P. Fischer, Phys. Rev. B **73**, 214429 (2006).
[31]E. Mengotti, L. J. Heyderman, F. Nolting, B. R. Craig, J. N. Chapman, L. Lopez-Diaz, R. J. Matelon, U. G. Volkmann, M. Klui, U. Rdiger, C. A. F. Vaz, and J. A. C. Bland, J. Appl. Phys. **103**, 07D509 (2008).
[32]X. K. Hu, S. Sievers, A. Müller, V. Janke, and H. W. Schumacher, Phys. Rev. B **84**, 024404 (2011).
[33]V. N. Krivoruchko and A. I. Marchenko, J. Appl. Phys. **109**, 083912 (2011).
[34]S. Tacchi, M. Madami, G. Gubbiotti, G. Carlotti, A. O. Adeyeye, S. Neusser, B. Botters, and D. Grundler, IEEE Trans. Magn. **46**, 1440 (2010).
[35]G. Gubbiotti, S. Tacchi, M. Madami, G. Carlotti, A. O. Adeyeye, and M. Kostylev, J. Phys. D: Appl. Phys. **43**, 264003 (2010).
[36]S. Neusser and D. Grundler, Adv. Mater. **21**, 2927 (2009).
[37]D. H. Y. Tse, S. J. Steinmuller, T. Trypiniotis, D. Anderson, G. A. C. Jones, J. A. C. Bland, and C. H. W. Barnes, Phys. Rev. B **79**, 054426 (2009).
[38]O. N. Martyanov, V. F. Yudanov, R. N. Lee, S. A. Nepijko, H. J. Elmers, R. Hertel, C. M. Schneider, and G. Schönhense, Phys. Rev. B **75**, 174429 (2007).
[39]M. Yu, L. Malkinski, L. Spinu, W. Zhou, and S. Whittenburg, J. Appl. Phys. **101**, 09F501 (2007).
[40]M. J. Pechan, C. Yu, R. L. Compton, J. P. Park, and P. A. Crowell, J. Appl. Phys. **97**, 10J903 (2005).
[41]C. Yu, M. J. Pechan, and G. J. Mankey, Appl. Phys. Lett. **83**, 3948 (2003).
[42]H. Kronmüller and M. Fähnle, *Micromagnetism and the Microstructure of Ferromagnetic Solids* (Cambridge University Press, Cambridge, UK, 2003).
[43]J. Fidler and T. Schrefl, J. Phys. D: Appl. Phys. **33**, R135 (2000).
[44]A. Vansteenkiste and B. Van de Wiele, J. Magn. Magn. Mater. **323**, 2585 (2011).
[45]L. J. Heyderman, S. Czekaj, F. Nolting, D.-H. Kim, and P. Fischer, J. Magn. Magn. Mater. **316** (2007).